Effects of charge doping on Mott insulator with strong spin-orbit coupling, Ba₂Na_{1-x}Ca_xOsO₆

Rong Cong 0, 1,* Erick Garcia, 1,* Paola C. Forino 0, 2 Anna Tassetti 0, 2 Giuseppe Allodi, 3 Arneil P. Reyes 0, 4
Phoung M. Tran, 5 Patrick M. Woodward, 5 Cesare Franchini, 2, 6 Samuele Sanna 0, 2, † and Vesna F. Mitrović 1, †

**Department of Physics, Brown University, Providence, Rhode Island 02912, USA

**Department of Physics and Astronomy "A. Righi", University of Bologna, I-40127 Bologna, Italy

**Dipartimento di Scienze Matematiche, Fisiche e Informatiche, Universitá di Parma I-43124 Parma, Italy

**National High Magnetic Field Laboratory, Tallahassee, Florida 32310, USA

**Department of Chemistry and Biochemistry, Ohio State University, Columbus, Ohio 43210, USA

**Faculty of Physics, University of Vienna, Vienna 1090, Austria

(Received 5 January 2023; revised 29 June 2023; accepted 31 July 2023; published 22 August 2023)

The effects of doping on the electronic evolution of the Mott insulating state have been extensively studied in efforts to understand mechanisms of emergent quantum phases of materials. The study of these effects becomes ever more intriguing in the presence of entanglement between spin and orbital degrees of freedom. Here, we present a comprehensive investigation of charge doping in the double perovskite Ba_2NaOsO_6 , a complex Mott insulator where such entanglement plays an important role. We establish that the insulating magnetic ground state evolves from canted antiferromagnet (cAFM) [Lu *et al.*, Nat. Commun. 8, 14407 (2017)] to Néel order for dopant levels exceeding $\approx 10\%$. Furthermore, we determine that a broken local point symmetry (BLPS) phase, precursor to the magnetically ordered state, occupies an extended portion of the (H-T) phase diagram with increased doping. This finding reveals that the breaking of the local cubic symmetry is driven by a multipolar order, most likely of the antiferro-quadrupolar type [Khaliullin *et al.*, Phys. Rev. Res. 3, 033163 (2021); Churchill and Kee, Phys. Rev. B 105, 014438 (2022)]. Future dynamical measurements will be instrumental in determination of the precise nature of the identified multipolar order.

DOI: 10.1103/PhysRevMaterials.7.084409

I. INTRODUCTION

Intricate interplay between strong electron correlations, and intertwined spin and orbital degrees of freedom leads to many diverse complex quantum phases of matter [1-5]. Often, correlations of the spin and orbital degrees of freedom can be treated on distinct energy scales. However, this is not the case in systems containing 5d transition-metal ions, where spin-orbit coupling (SOC) and electron correlations are comparable in size [2,6-12]. As a result, 5d compounds exhibit a wide range of exotic magnetic properties, structural distortions, and multipolar ordering [1,13-21]. The underlying physical ground state, is controlled by the multiplet structure of the constituent ions, the nature of the chemical bonds in the crystal, and its symmetry. This complexity often leads to intricate quantum "hidden" orders, elusive to most standard experimental probes. Nevertheless, the structural, magnetic, and electronic properties can be finely tuned by altering the degeneracy of a multitude of ground states varying external perturbations, such as pressure, strain, and doping [20,22–24].

The expectation, under the simplest picture, is that Mott insulators with integer number of electrons per site favor an

antiferromagnetic ground state (AFM), and that charge doping leads to a metal-insulator transition (MIT) into a conducting state [25]. The most notable example of doping is the superconducting state in cuprates believed to emerge from a parent antiferromagnetic Mott state [26–28]. Specifically, as doping increases, antiferromagnetism gives way to exotic orders such as "stripe", unidirectional charge density wave, spin-density wave, and unconventional d-wave superconductivity and with high enough doping the system becomes a Fermi liquid [26,28,29]. In addition to this well known class of MITs induced in Mott insulators by Coulomb interactions [26,27,30–32], insulators purely driven by spin correlations have been recently observed [33]. Yet another interesting case arises in Mott insulators when a strong SOC locally entangles the spin and orbital degrees of freedom. In such systems unconventional quantum magnetic and multipolar orders may emerge [2,3,16,17,22]. Furthermore, the effects of charge doping are expected to be strikingly different than in systems where SOC can be treated as a perturbation to electronic correlations [2,34–40], because multipolar orbital order and/or complex multiorbital arrangements favor charge localization. A representative material of such Mott insulators is the $5d^1$ double perovskite Ba₂NaOsO₆ [41,42] that evolves to the $5d^2$ configuration upon charge doping.

This $5d^1$ Os⁷⁺ Mott insulator displays a seemingly contradictory combination of a weak ferromagnetic moment ($\sim 0.2 \, \mu_B$ /formula unit) below $T_C \approx 6.8$ K and a negative Weiss temperature [43]. Its weak moment at low-temperature

^{*}These authors contributed equally to this work.

[†]s.sanna@unibo.it

[‡]vemi@brown.edu

derives from an exotic canted-antiferromagnetic (cAFM) phase that is preceded by a broken local point symmetry (BLPS) state [13,44,45]. Fully doped, Ba₂CaOsO₆, on the other hand, is a $5d^2$ Os⁶⁺ Mott insulator that possibly hosts a complex ferro-octupolar order instead of a simple Néel AF order [16,21,21,46,47]. Interestingly, recent theoretical work reveals different types of multipolar orders in $5d^2$ Mott insulators, such as ferri-octupolar [48], ferro-octupolar [22,49], and antiferro-quadrupolar ordering [18,50]. Microscopic study of the magnetic and structural properties of the double-perovskite 5d compounds with cubic symmetry, as presented here, provides essential guidance for the development of the relevant theoretical framework for the description of Mott insulators with strong SOC. Once identified, such a theoretical framework can be extended to more intricate lattices, such as the honeycomb and/or triangular lattice, where novel types of exotic quantum orders can be stabilized [2,12,50].

Here, we present a comprehensive study of the effect of charge doping on a Mott insulator with both strong electron correlations and SOC, represented by the double perovskite Ba₂NaOsO₆, from $5d^1 \rightarrow 5d^2$. Specifically, we investigate the magnetic field-temperature (H-T) phase diagram evolution as a function of charge doping (x) achieved by Na^+/Ca^{2+} heterovalent substitution in Ba₂Na_{1-x}Ca_xOsO₆, employing nuclear magnetic resonance (NMR), muon spin spectroscopy (μSR) , and magnetization measurement techniques. We find that the system remains insulating at all doping levels, implying that the dopants form an inhomogeneous electronic state [23]. We compiled a magnetic and structural phase diagram for dopant concentrations ranging from $x = 0 \rightarrow 1$. We point out that in this paper we exploited ²³Na nuclear spins, which thus precluded the investigation of pure $5d^2$, i.e., (x = 1), compound by NMR. The insulating magnetic ground state evolves from canted antiferromagnetic (AF) [13] to Néel nearly collinear AF state (hereafter referred to as collinear AF state for brevity) for dopant levels exceeding \approx 10%. Analyzing the complex broadening of the ²³Na NMR spectra, which onsets well above the magnetic transition, and temperature dependence of NMR shift, we establish that a cubic to orthorhombic local distortion of the O-octahedra is present for all compositions [51,52]. The local distortion is the signature of a BLPS phase, identified as a precursor to the magnetic state in the single crystals of Ba₂NaOsO₆ [13], and not a trivial consequence of a simple structural phase transition. The observation of the breaking of the local cubic symmetry and concurrent development of the NMR shift anisotropy for the entire range of dopings investigated implies that this symmetry breaking is driven by a multipolar order, most likely of the antiferro-quadrupolar type [18,50]. Remarkably, we find that the cubic to orthorhombic local distortion occurs independently of the exact nature of the low-temperature magnetic state, signaling that the presence of canted moments is not the sole consequence of the BLPS [53]. In summary, our findings evidence that local distortions persist in the doped samples and that they favor the onset of an antiferro-quadrupolar order.

In this paper, we describe details of our experimental approach and data analysis in Sec. II. More precisely, we outline main features of μ SR, magnetization, and NMR measure-

ments and their respective data analysis. In Sec. III, we present findings of our systematic study of Ba₂Na_{1-x}Ca_xOsO₆ and effects of doping in the Os based Mott insulator. We discuss physical implication of our findings in Sec. IV. Following the main text, we provide appendices, which outline important, but tedious, details of data analysis and modeling: the Curie-Weiss behavior (Appendix A), hyperfine tensor form (Appendix B), and simulations of the NMR spectra (Appendices C and D).

II. EXPERIMENTAL TECHNIQUES AND MODELING METHODS

The powder samples of $Ba_2Na_{1-x}Ca_xOsO_6$ investigated here are the same as in Ref. [23]. Powder x-ray diffraction (PXRD) measurements were performed to test the quality of the samples and analyzed with Rietveld refinement. The compositional evolution of the lattice parameter is shown to follow Vegard's Law, indicating a successful Na/Ca substitution [23].

A. Muon spin spectroscopy - μ SR

All μ SR measurements were performed at the General Purpose Surface-Muon Instrument at the Paul Scherrer Institute in Switzerland. In μ SR measurements, spin-polarized muons implant in the powder samples and precess around the local magnetic field with a frequency given by $\nu = \gamma_{\mu} \cdot |\mathbf{B}|/2\pi$, where $\gamma_{\mu} = 2\pi \times 135.5$ MHz/T. The muons decay with a characteristic lifetime of 2.2 μ s, emitting a positron, preferentially along the direction of the muon spin. The positrons are detected and counted by a forward $[N_F(t)]$ and backward detector $[N_B(t)]$, as a function of time. The asymmetry function A(t) is given by

$$A(t) = \frac{N_B(t) - \alpha N_F(t)}{N_B(t) + \alpha N_F(t)},\tag{1}$$

where α is a parameter determined experimentally from the geometry and efficiency of the μ SR detectors. A(t) is proportional to the muon spin polarization, and thus reveals information about the local magnetic field sensed by the muons. A typical μ SR spectra in zero-field (ZF) condition (i.e., in external field H = 0) below and above the magnetic transition temperature for Ba₂Na_{1-x}Ca_xOsO₆ are presented in Fig. 1(a). That is, we plot the temperature dependence of the μ SR asymmetry for x = 0 as a representative set of data. The paramagnetic (PM) state depicted in green is observed at the higher temperature ($T = 15 \,\mathrm{K}$). The oscillations observed at low temperature depict the precession of muons about the local magnetic field deriving from long-range magnetic ordering. The μ SR spectrum at the base temperature is in a very good agreement with previous measurements performed on a Ba₂NaOsO₆ single crystal [42]. The μ SR spectra for all doping concentrations display damped oscillations at low temperatures [Fig. 1(b)]. The appearance of these damped oscillations marks a transition to a state of long-range magnetic order. Specifically, we show in Fig. 1(b) that long-range magnetic ordering develops at low temperatures throughout the entire doping regime. Furthermore, the nature of the magnetic ordering is probed by magnetization and NMR

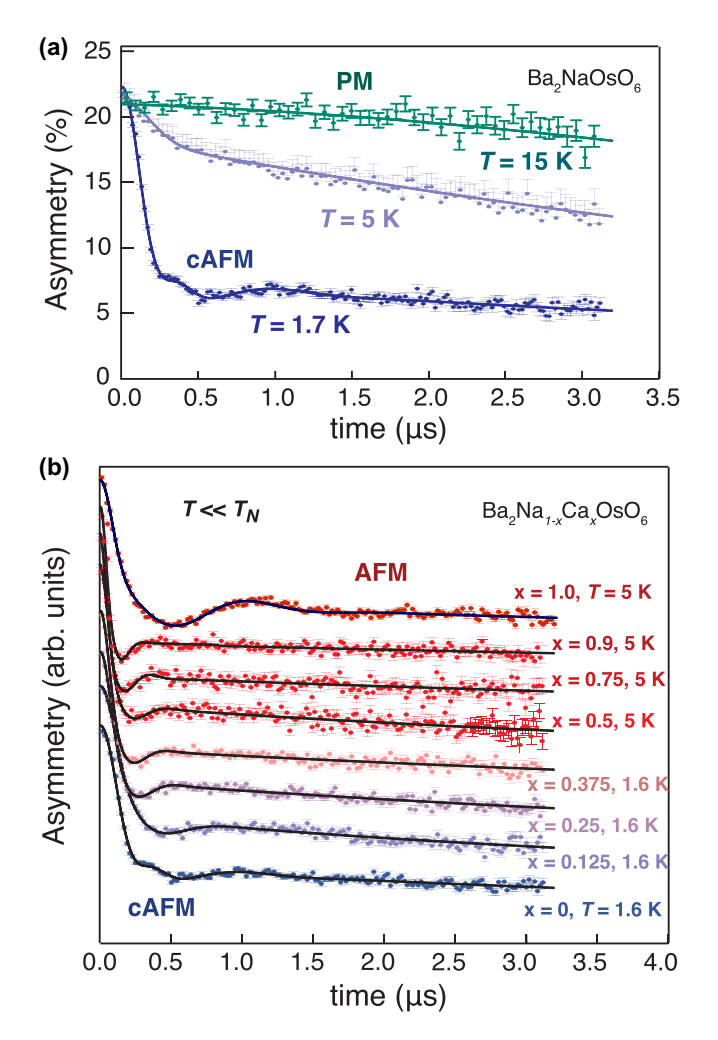


FIG. 1. Representative zero-field μ SR data. (a) Temperature evolution of muon asymmetry with decreasing temperature for x=0. (b) Asymmetry for all doping concentrations at low temperatures ($T \in [1.6 \text{ K}, 5 \text{ K}]$), well below the magnetic ordering. In this case, the vertical axis are offset for clarity. Solid lines are results of the asymmetry fit to Eq. (2). Blue colors denote a canted antiferromagnetic (cAFM), red an antiferromagnetic (AFM), and green paramagnetic (PM) phase.

measurements, as described in Secs. III B and III C. Although oscillations might seem insignificant, beyond approximately 1.5 microseconds, clear μ SR evidence for magnetic order is provided by the strong decay/dephasing of the signal. Indeed, the strong decay/dephasing of the μ SR signal allows us to precisely determine the magnetic volume fractions, as we discuss in the next paragraph.

The spectra for the end members, x = 0 and x = 1, are in agreement with those previously reported [42,47]. Each individual spectrum was fitted to a sum of precessing and relaxing asymmetries given by

$$A(t) = \left[\sum_{i=1}^{2} A_i e^{-\frac{\sigma_i^2 t^2}{2}} \cos(2\pi v_i t) + A_3 e^{-\frac{\sigma_3^2 t^2}{2}} \right] + A_{\ell} e^{-\frac{t}{T_1}}. \quad (2)$$

The terms inside the brackets reflect the perpendicular component of the internal local field probed by the spin-polarized muons, the first term corresponds to the damped oscillatory

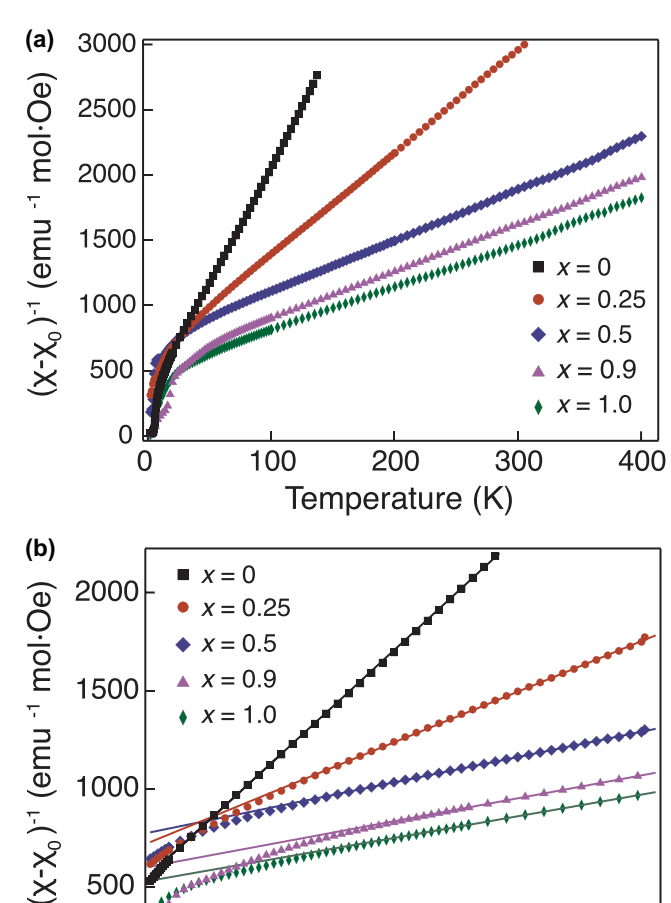


FIG. 2. Representative temperature dependence of zero-field cooled magnetic susceptibility. (a) High-temperature range of magnetic susceptibility. (b) Low-temperature range of magnetic susceptibility with linear Curie-Weiss fittings in the PM state.

60

80

Temperature (K)

20

40

muon precession about the local internal fields at frequencies v_i , while the second reflects a more incoherent precession with a local field distribution given by σ . The term outside the brackets reflects the longitudinal component characterized by the relaxation rate T_1 . The fitting results are displayed as solid lines in Fig. 1.

The development of a magnetic phase can be probed by measuring the volume of magnetic and nonmagnetic regions within our sample. This magnetic volume fraction $(V_{\rm mag})$, plotted in Fig. 3(a), is given by the expression

$$V_{\text{mag}} = \frac{3}{2} \left(1 - \frac{A_{\ell}}{A_{\text{tot}}} \right). \tag{3}$$

120

140

100

Therefore, the magnetic volume fraction can be obtained from the analysis and data plotted in Fig. 1, by extracting longitudinal (A_{ℓ}) and total (A_{tot}) component of the polarized muons.

B. Magnetization

Bulk magnetization measurements were performed using a superconducting quantum interference device (SQUID)

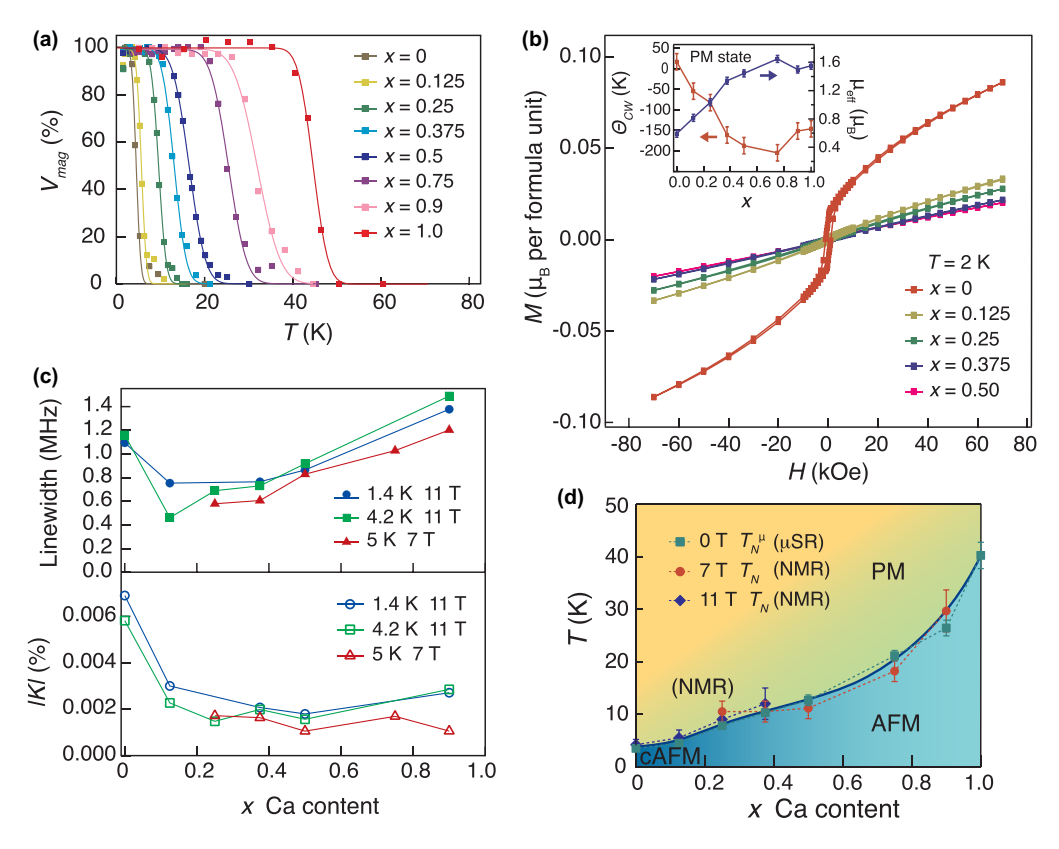


FIG. 3. Magnetic state evolution as a function of charge doping (x) in $Ba_2Na_{1-x}Ca_xOsO_6$. (a) Magnetic volume fraction extracted from μ SR asymmetry for all doping levels. The magnetic transition temperature is defined as the 90% filling of the magnetic volume and increases monotonically with increasing Ca doping. (b) Magnetization as a function of applied magnetic field at 2 K. The results of high-temperature $(T \gtrsim 50 \text{ K})$ Curie-Weiss fittings for magnetic susceptibility measurements in the PM state are shown in the inset. (c) ²³Na NMR spectral linewidth (top) and absolute value of Knight shift (bottom) as a function of doping concentration at various temperatures. (d) Magnetic phase diagram. Markers denote magnetic transition to the canted AFM and collinear AFM state for zero-field μ SR and high-field NMR measurements. Solid line serves as a guide to the eye. Typical error bars are on the order of a few percent and not shown for clarity in panels (a)–(c).

magnetometer. Isothermal magnetization measurements as a function of applied field were performed at 2 K from -70 to 70 kOe. Zero-field and field-cooled magnetic susceptibility (χ) measurements were performed from 2 to 400 K under an applied field of 1000 Oe.

The $\chi(T)$ data in the paramagnetic region fits well a Curie-Wiess law with addition of a temperature-independent constant χ_0 term. That is, data for all the concentrations is fitted to the following expression: $\chi = \chi_0 + C/(T - \Theta_{\rm CW})$, with the Curie constant (C) and the Curie-Wiess temperature $(\Theta_{\rm CW})$ as fitting parameters. Representative examples of the resulting $(\chi - \chi_0)^{-1}(T)$ curves are reported in Fig. 2(b), we highlight the low-temperature range of the data and include linear Curie-Weiss (CW) fittings in the PM state $(T \gtrsim 50 \text{ K})$. The individual CW fittings are shown in Appendix A. This data and fits were used to extract CW temperature $(\theta_{\rm CW})$ and effective moment per formula unit $(\mu_{\rm eff})$ as described in Sec. III B and illustrated in the inset to Fig. 4(b).

C. NMR

NMR measurements were performed using high homogeneity superconducting magnets at Brown University, and the National High Magnetic Field Laboratory in Tallahassee,

FL for magnetic fields exceeding 9 T. Temperature control was provided by 4 He variable temperature inserts. 23 Na NMR data ware collected using state-of-the-art, laboratory-made NMR spectrometers from the sum of spin-echo Fourier transforms recorded at constant frequency intervals. Pulse sequences of the form $(\pi/2 - \tau - \pi/2)$ were used and none of the presented NMR observables depend on the duration of time interval τ .

 23 Na NMR is a powerful local probe of both the electronic spin polarization (local magnetism), via the hyperfine coupling between electronic magnetic moments and the 23 Na nuclear spin I=3/2, and the charge distribution (orbital order and lattice symmetry), via the quadrupolar interaction between the electric field gradient (EFG) and the 23 Na quadrupole moment Q [13,51]. They affect both the first and second moments of the frequency distribution, i.e., the NMR spectra.

The Knight shift is defined as

$$K^i = (\omega^i - \omega_0)/\omega_0,$$

where $\omega_0 = ^{23}\gamma \cdot H_0$, where $^{23}\gamma = 11.2625$ MHz/T and H_0 is the externally applied magnetic field, and ω^i is obtained from the first moment and/or peak position of the NMR spectral lines. This equation forms the general definition of

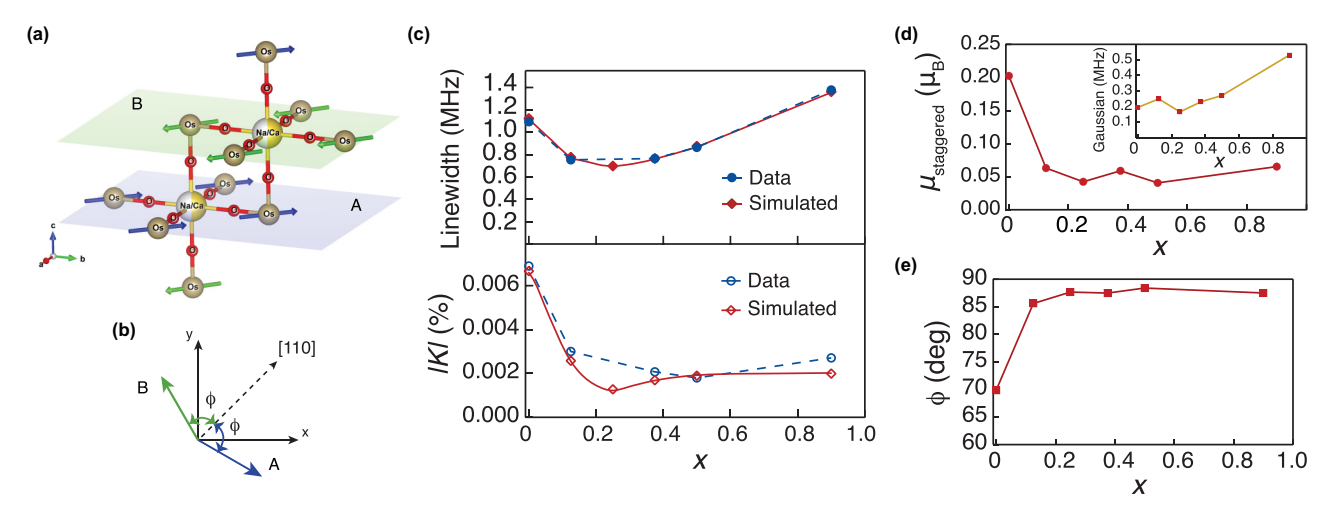


FIG. 4. Doping evolution of the staggered moment in the low-temperature magnetic state. (a) Schematic of the spin model used to fit the NMR observables. Different colors of the arrows denote different spin environments at the Os sites. The two planes with distinctly oriented moments from sublattice A and B are shown in different shades. (b) Schematic of the canted spin arrangement by angle ϕ with respect to the [110] direction in the XY plane. (c) Simulated and measured NMR spectra linewidth and Knight shift at T = 1.4 K and H = 11 T as a function of Ca doping x in Ba₂Na_{1-x}Ca_xOsO₆. (d) Simulated evolution of the staggered moment, defined as the projection of moments from two sublattices, A and B, along the applied field, as a function of doping in the magnetic state. The Gaussian blur, used to properly account for magnetic broadening, of simulated spectra is shown in the inset. The blur increases abruptly for x = 0.9. This might be related to the increased inhomogeneity of the local magnetic field environment at the Na nuclei site. Details of this simulation can be found in Sec. II D and Appendix D. (e) Simulated evolution of the canted angle, defined as the angle between the sublattice FM spin orientation and the [110] easy axis, as a function of doping in the magnetically ordered state. Typical error bars are on the order of a few percent and not shown for clarity.

the NMR shift K in terms of the observed NMR frequency, $\omega^i \equiv \gamma H_0(1+K)$, where $K \equiv H_{\rm loc}/H_0$ is the shift. Therefore, K is a measure of the relative strength of the component of the local magnetic field ($H_{\rm loc}$) parallel to the applied magnetic field, H_0 . In the more general case where the shift varies as a function of the orientation of H_0 (anisotropic shift), the scalar K is promoted to a second-rank tensor \mathbb{K} and the expression for the observed NMR frequency becomes [54]

$$\omega^i = \gamma H_0(1 + \hat{\mathbf{h}} \cdot \mathbb{K} \cdot \hat{\mathbf{h}}), \tag{4}$$

where $\hat{\mathbf{h}} = \mathbf{H}_0/H_0$ is a unit vector in the direction of the applied magnetic field.

When the quadrupole interaction is taken into account, the observed NMR frequency becomes $\omega^i = \gamma(1+K)H_0 + \omega_Q(m-1/2)(3\cos^2\theta_Q-1+\eta\sin^2\theta_Q\cos 2\varphi_Q)$ up to second order in perturbation theory [13,51,54]. The second term accounts for the quadrupole interaction for each $m\leftrightarrow m\pm 1$ transition and can be used to deduce the quadrupole parameters when the principal axes of the EFG tensor coincide with those of the crystal, as in the case of Ba₂NaOsO₆ [13]. Here, θ_Q and φ_Q are the angles between the applied field and the principal axes of the electric field gradient (EFG) defined so that $|V_{ZZ}| \geqslant |V_{XX}| \geqslant |V_{YY}|$ and $eq \equiv V_{ZZ}$. The asymmetry parameter η is set as $\eta \equiv (V_{XX} - V_{YY})/V_{ZZ}$. The quadrupolar frequency equals to $\omega_Q = 3e^2qQ/(\hbar 2I(2I-1))$, where Q and Q are the nuclear and electronic quadrupole moments.

To relate the quadrupolar interaction effect to the observed NMR frequency, we introduce the quadrupolar splitting tensor \mathbb{W} , such that $\Delta \omega = \sum_{\alpha} W_{\alpha} \hat{h}_{\alpha}^2$ in the coordinate system O_{xyz} , where \mathbb{W} is diagonal. Here O_{xyz} is defined by the crystalline axis of the cubic perovskite unit cell [51], $\alpha = \{x, y, z\}$, and \hat{h} is the unit vector along the applied field.

In the presence of the anisotropic shift and quadrupolar interactions, the full expression for the observed NMR frequency becomes

$$\omega^{i} = \gamma H_{0}(1 + \hat{\mathbf{h}} \cdot \mathbb{K} \cdot \hat{\mathbf{h}} + \mathbb{W} \cdot \hat{\mathbf{h}}^{2}). \tag{5}$$

This most general expression is then used to extract the relative strength of the components of the local magnetic field (H_{loc}) projected along the applied magnetic field direction from the measurements of the Knight shift.

D. Calculation of NMR spectra below T_N

In the magnetically ordered phase, we model the local magnetic field at a Na site as $H_{loc} = \hat{\mathbf{h}} \cdot \sum_{i} \mathbb{A}_{i} \cdot \vec{S}_{i}$, where $\hat{\mathbf{h}}$ is a unit vector in the applied field direction, A_i is the hyperfine coupling tensor with the ith nearest-neighbour Os atom, and \hat{S}_i is its local spin moments. We note that contributions from dipolar effects are relatively small and are thus neglected. By performing a full lattice sum, we calculate the local fields projected in the direction of the applied field at the Na sites for the entire single crystal. The corresponding NMR spectra is a histogram of these local fields. The powder spectrum is then obtained by rotating the $\hat{\mathbf{h}}$ over the solid angle and integrating the results (see Appendix D). The diagonal components of the hyperfine tensor are optimized based on the hyperfine coupling values obtained from the NMR Knight shift and magnetic susceptibility measurements (see Appendix B), while the symmetry of the hyperfine tensor is assumed to be the same as that found in the single crystal Ba₂NaOsO₆ [13]. The quadrupolar broadening effects are accounted for utilizing EFG parameters determined from the intermediate temperature powder spectrum simulation (Appendix D).

E. Determination of transition temperatures

The transition temperature (T_N) from the PM to low-temperature magnetically ordered state was determined by examining the magnetic volume fraction $V_{\rm mag}$ from zero-field μ SR, and in finite fields from the temperature dependence of the NMR observables. That is, T_N^{μ} is delineated as a temperature at which $V_{\rm mag}$ exceeds 90%. From NMR analysis, T_N is defined as the onset temperature of a significant drop in the Knight shift associated with the formation of the AF ordering. Such T_N is consistent with the one determined from the peak of the NMR relaxation rate (not shown), induced by critical fluctuations when approaching a transition into a long-range ordered magnetic state as a function of temperature.

The onset temperature for the detectable breaking of local cubic symmetry, T_{SB} , was identified by the bifurcation in 1/|K| vs T between the shifts defined relative to ω^i , corresponding to the peak position (i = pp) and first moment (i = fm). We point out that T_{SB} does not denote true phase transition temperature, but it rather refers to the temperature below which magnitude of local distortions becomes detectable (i.e., static within the measurement time window of $\gtrsim 1 \,\mu s$) by our NMR experiments. Moreover, the extension of the room temperature x-ray absorption fine structure (EX-AFS) investigation of local structure evolution with doping Ref. [23] to low temperatures in the BLPS phase, as identified by NMR, found no evidence of the breaking of the local cubic symmetry at the Na site. Therefore, distortions reported here are below sensitivity limit for x-ray absorption spectroscopy reported in Ref. [23].

III. RESULTS

We now describe the main findings of our systematic study of $Ba_2Na_{1-x}Ca_xOsO_6$ through the partial heterovalent substitution of monovalent Na with divalent Ca for $0 \le x < 1$, performed to better understand the effects of doping and to elucidate the competing interactions that drive distinct magnetic ground states utilizing muon spin relaxation (μSR), nuclear magnetic resonance (NMR), and magnetization measurements. We find that the insulating state persists at all doping concentrations despite the injection of electrons and an evolution into the AFM state. This finding is based on thorough examination of the response of the NMR resonant circuit.

A. Magnetic state-μSR magnetic volume fraction

First, we consider the evolution of the magnetic ground state of $Ba_2Na_{1-x}Ca_xOsO_6$ as a function of the Na/Ca substitution ($0 \le x \le 1$) as probed by zero-field muon spin relaxation (ZF- μ SR) measurements. In the absence of an external field (H=0 T), the spin I=1/2 muon implanted in the sample precesses around the spontaneous local magnetic field arising from the magnetically ordered state at the muon site. The muon precessions are reflected in damped oscillations of the muon asymmetry decay, probing the fraction of precessing muons, which in turn is proportional to the magnetic volume, as described in Sec. II A. Our ZF- μ SR asymmetry measurements for the end members x=0 and 1 are in agreement with those previously reported in Refs. [42,48]. In Fig. 3(a), we plot the temperature evolu-

tion of the magnetic volume fraction $V_{\rm mag}$ as a function of doping. We find that samples of all concentrations display a magnetic transition as the volume fraction approaches 100% in the low-temperature limit. The transition temperature into a magnetically ordered state T_N^{μ} defined to be at $V_{\rm mag} = 90\%$, grows monotonically from approximately T = 5 K to 40 K as increasing doping induces a configuration change from the $5d^1$ to the $5d^2$ Ref. [23], as illustrated in Fig. 3(d).

B. Magnetic state-magnetization

We have also performed magnetization measurements to get a better insight into the nature of the magnetic transitions observed through ZF- μ SR. In Fig. 3(b), we plot magnetization curves as a function of an applied magnetic field for T = 2 K. The x = 0 sample displays a nonlinear field dependence with a characteristic S shape and a small hysteretic behavior consistent with a moderately weak ferromagnetic character due to the significant moment canting in the cAFM phase. This is in agreement with the magnetization behavior observed in Ba₂NaOsO₆ single crystals [43]. This hysteretic behavior is rapidly concealed with charge doping and is effectively undetectable for doping exceeding $x \sim$ 0.1. Magnetic susceptibility measurements were performed as a function of temperature at H = 0.1 T for all samples. As described in Sec. IIB, the resulting magnetic susceptibility $[\chi(T)]$ in the high-temperature paramagnetic (PM) region fits well to a Curie-Weiss (CW) function plus a small temperature-independent contribution (Fig. 2). The resulting CW temperature (θ_{CW}) and effective moment per formula $(\mu_{\rm eff})$ are displayed in the inset to Fig. 3(b). The values of the end members are in very good agreement with those previously reported for Ba₂Na_{1-x}Ca_xOsO₆ at x = 0 ($\mu_{eff} =$ $0.6 \mu_B$) and $x = 1 \ (\mu_{\text{eff}} = 1.6 \mu_B) \ [41,43,46,47]$. Furthermore, the extracted effective moments increase smoothly as the system evolves from the $5d^1$ to $5d^2$ configuration, while $\theta_{\rm CW}$ becomes more negative. The extracted effective moment for both configurations is significantly suppressed from the theoretical value expected if SOC were negligible ($\mu_{\rm eff}$ = $1.73 \,\mu_B$ and $\mu_{\rm eff} = 2.83 \,\mu_B$ for $5d^1$ to $5d^2$ configurations, respectively) and is closer to the expected moments in the infinite SOC limit ($\mu_{\text{eff}} = 0 \,\mu_B$ and $\mu_{\text{eff}} = 1.25 \,\mu_B$ for $5d^1$ and $5d^2$ configurations, respectively) [6,7,55]. The experimentally determined values of $\mu_{\rm eff}$ being significantly reduced from those expected for negligible SOC limit indicates the presence of strong SOC (in agreement with predicted SOC coupling lambda $\sim 0.3 \,\mathrm{eV}$), while their being larger than those in the limit of infinite SOC can be attributed to the hybridization of Os d and oxygen p orbitals, with extra moments coming from the p orbitals, in agreement with predictions of Ref. [56]. The most likely origin of the observed effective moment increase with doping $(5d^1 \rightarrow 5d^2)$ is the enhancement of the spin quantum number. This is because the spin (S) is predicted to increase from S = 1/2 to S = 1 as doping changes from $x = 0 \rightarrow x = 1$ [56].

C. Magnetic state-NMR

In order to obtain insight into the microscopic nature of the magnetically ordered state throughout the doping evolution,

we performed detailed analysis of the ²³Na NMR spectra following the methods outlined in Secs. II C and II D. That is, we analyzed how the spectral shape changes in the magnetically ordered state, i.e., measured below T_N , as a function of the Ca content x. In Fig. 3(c), we plot the absolute value of the Knight shift, deduced from first moment of the NMR spectra (Fig. 11 in Appendix D), and the linewidth of the spectra as a function of x. The magnitude of the Knight shift rapidly decreases on introduction of Ca dopants (x > 0) and remains nearly constant for higher doping ($x \ge 0.1$). The absolute value of the shift is a measure of the local magnetic moment projected along the external magnetic field direction. In the magnetically ordered canted state, the shift is proportional to the projection of the noncompensated magnetic moment along the applied magnetic field, as was demonstrated by ²³Na NMR measurements on Ba₂NaOsO₆ single crystals [13,44]. Therefore, the observed abrupt decrease of the shift upon the introduction of dopants indicates that the addition of charge effectively quenches the FM component, while further doping $(x \ge 0.1)$ leads to a more uniform distribution of the projected moments. Furthermore upon the introduction of dopants (x >0), the linewidth, which reflects the distribution of the magnetic fields projected along the applied magnetic field, exhibits the same abrupt decrease as the NMR shift, in agreement with the suppression of the canted nature of the magnetic order upon charge doping. In the collinear AFM state, the spectral linewidth is qualitatively proportional to the size of the local ordered magnetic moment. Thus, the smooth increase of the linewidth observed for x > 0.1 in Fig. 3(c), indicates a progressive rise of the ordered magnetic moment as the charge concentration approaches x = 1, i.e., the $5d^2$ configuration (full quantitative analysis of the linewidth is presented in the next section).

We point out that one would naively expect that the linewidth either to monotonically increase with doping since it introduces inhomogeneity in the crystal or to display a maximum at 50% where the chemical disorder is maximized. Neither of these possibilities accounts for our observations here, because the NMR linewidth reflects intrinsic inhomogeneities of the magnetic ground state. Both the magnetization and the low-temperature NMR measurements are consistent with a picture where the canted magnetic state rapidly evolves into the collinear AFM phase upon the introduction of charge and that the ordered magnetic moment increases as a function of Ca doping.

IV. DISCUSSIONS

A. Microscopic nature of the magnetic state

To investigate the direct effect of doping on the nature of the staggered magnetic moments, i.e., a two-sublattice canted antiferromagnetic order observed in Ba₂NaOsO₆ single crystal [13], we have simulated the powder spectrum corresponding to the two sublattice cAFM order identified in Ref. [13] (Sec. II D and Appendix D). The input parameters for the simulations include the electronic spin moment (\vec{S}) and the hyperfine coupling tensor (\mathbb{A}). For each Ca doping concentration, we fix the value of \vec{S} to be that of the effective moment ($\vec{S} = \mu_{\rm eff}$) deduced from susceptibility measurements [the

inset to Fig. 3(b)]. Simulated spectra are then fitted to the observed ones with canting angle, and consequently staggered moment, as a fitting parameter. Here, the canting angle is that between the sublattice FM spin orientation and the [110] easy axis, while the staggered moment refers to the projection of the moments from the two sublattices, A and B, along the applied field direction. The simulation results are summarized in Fig. 4. We find that both, the canting angle and the staggered moment, change abruptly upon charge doping for x > 0.1. For x = 0, we obtain the best fit for a canting angle of 68° , consistent with that reported for pure Ba₂NaOsO₆ single crystal [13]. For x > 0.1, the canting angle rapidly approaches 90°, the value associated with a collinear AFM state [see Fig. 4(d)]. The deduced canting angles and staggered moments serve as input parameters to calculate the doping evolution of the Knight shift and linewidth associated with the local spin arrangement depicted in Fig. 4(a). The calculated evolution of the shift and the linewidth is in an excellent agreement with observations, as shown in Fig. 4(c). As x increases, the Knight shift decreases as a direct consequence of the increase of the canting angle, as depicted in Fig. 4(b). On the other hand, the linewidth decrease with increasing x is associated with the weakening of the off-diagonal components of the hyperfine coupling tensor, for the canting angle ~90°. Furthermore, in the inset to Fig. 4(d) we plot the Gaussian blur, which is used to account for the inhomogeneous magnetic broadening of the measured spectra, and its abrupt increase with doping approaching $x \to 1$ indicates that injected charge is inhomogeneously distributed. More importantly, such abrupt increase in the linewidth close to pure $5d^2$ limit is predicted in the recent comprehensive theoretical study of effects of the impurity doping in the cubic double perovskites [57]. While the ab initio calculations indicate robustness of the ideal Ba₂CaOsO₆ against spontaneous lattice distortions, partial substitution of Ca²⁺ with Na⁺ induce local strains, which break point group symmetry around neighboring Os sites. These local strains break the degeneracy of the T_{2g} orbitals at the Os sites. While local/global strains can occur due to quadrupole order, they can also be present simply as impurity induced strain fields. Then at lower temperature, when octupolar order sets in, deviations from octahedral symmetry induce weak dipolar moments whose magnitude precisely tracks the octupolar order parameter. The direction of these dipole moments, being determined by the random strain fields is, however, still random, which causes the dramatic broadening of the spectrum. The observed increase of the linewidth, and Gaussian blur as $x \to 1$ can then be explained by strain field induced multipolar order predicted in Ref. [57]. Nevertheless, we cannot identify the exact nature, ferro-octupolar vs antiferro-quadrupolar, of the multipolar order as $x \to 1$. This is because the decay of the Knight shift and concurrent increase of the linewidth might be alternatively explained by the appearance of octupoles substituting the canted ferromagnetic order. These octupolar moments generate spatially nonuniform rapidly decaying magnetic field. Inhomogeneous octupolar fields could in turn cause visible line broadening. At the same time, since this multipolar phase is a ferrooctupolar phase, this field will be a sum of contributions from all neighboring sites. Since the precise spatial variation and these octupolar moment is quantitatively unknown, we are not

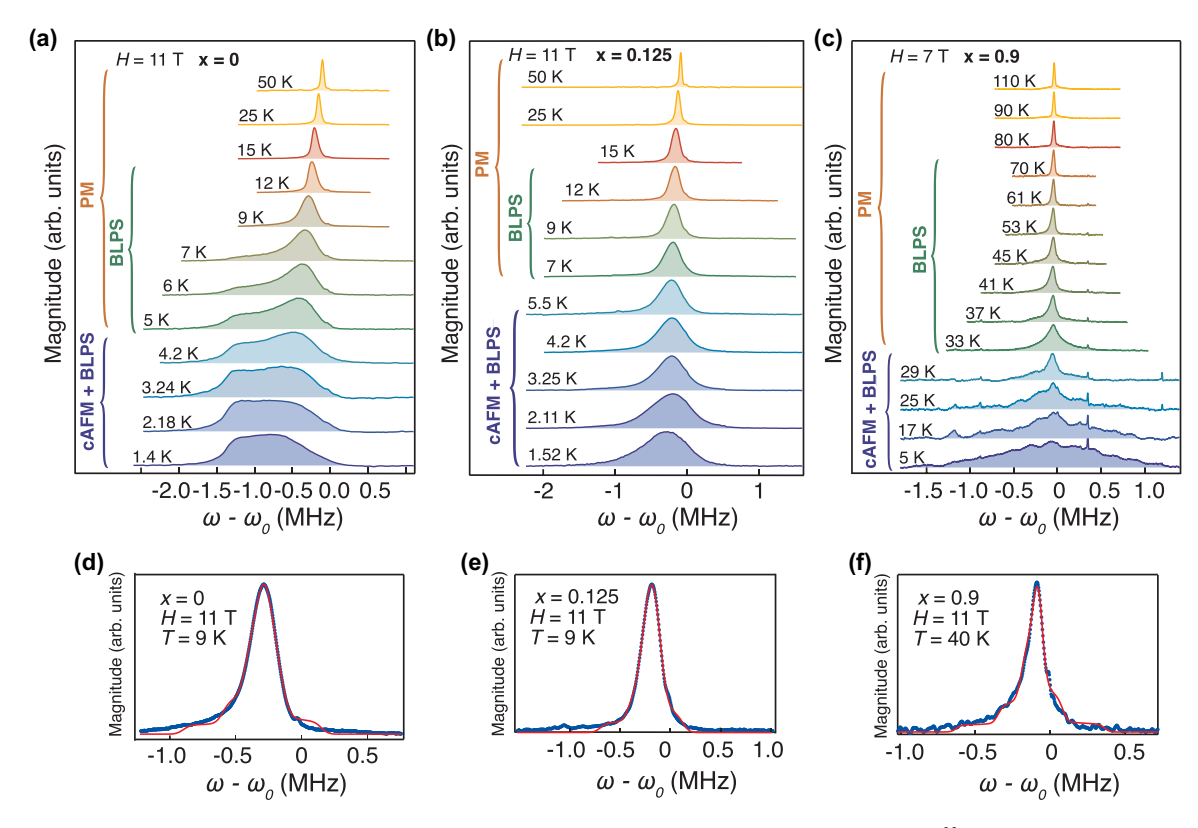


FIG. 5. NMR spectral evidence of broken local point symmetry. [(a)–(c)] Temperature evolution of 23 Na spectra for (a) x = 0, (b) x = 0.125, and (c) x = 0.9. [(d)–(f)] 23 Na powder NMR spectrum simulation results at H = 11 T for (d) x = 0, (e) x = 0.125, and (f) x = 0.9 in the BLPS phase.

able to confidently identify the exact nature of the multipolar order.

B. Broken local point symmetry (BLPS)

Next, we investigate the effect of charge doping on the BLPS phase identified in Ref. [13] through investigation of the NMR linewidth broadening, as illustrated in Figures 5(a)–5(c). In this paper, the onset temperature of the visible broken local point symmetry is determined from the NMR Knight shift as described in Sec. II E. To verify consistency of our two approaches employed to identify BLPS and to determine the nature of the local crystal symmetry, we then proceed to analyze NMR powder spectral shapes at temperatures above the transition to the magnetically ordered state.

This subtle symmetry breaking has eluded previous diffraction measurements [43], but is well reflected in the distortion of the NMR spectra by the unbalanced spectral weight distributed towards a lower frequency with respect to its main peak associated with the cubic symmetry (see Fig. 5). A direct phenomenological way to detect and estimate the distortion of the spectra is by comparing the temperature evolution of the frequency of the peak position of the spectra to the first moment of the frequency distributions. In Fig. 6, we display representative data sets for the comparison of the Knight shift obtained relative to the frequency ω^i of the first moment (i = fm) and peak (i = pp) of our NMR spectral lines (see Sec. II C). The clear bifurcation in 1/|K| between the shift obtained by using the peak position and first moment marks

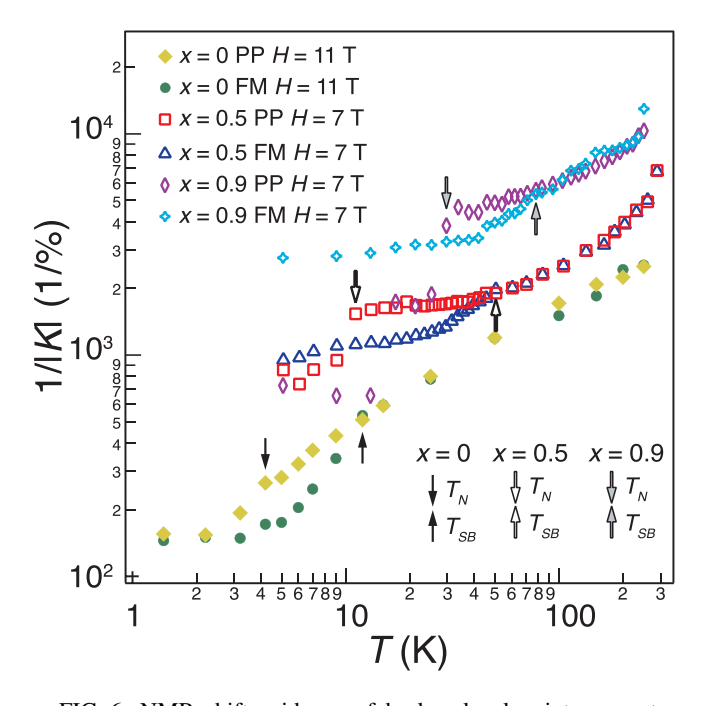


FIG. 6. NMR shift evidence of broken local point symmetry. Representative NMR Knight shift as a function of temperature at 11 T and 7 T. Arrows indicate the corresponding structural T_{SB} and magnetic T_N transition temperatures. x = 0.9 (Ca = 90%) data is vertically offset for presentation clarity. Typical error bars are on the order of a few percent and not shown for clarity.

the structural phase transition to the BLPS phase T_{SB} . Upon further cooling, a sharp drop of 1/|K| is observed, denoting the transition temperature T_N into the magnetic state (see Sec. II E). The magnetic transition temperature T_N obtained from the $1/|K^{pp}|$ drop, is consistent with that determined from the peak of the NMR relaxation rate (not shown) and from ZF-muSR measurements [Fig. 3(d)]. These observations indicate that below T_N , an AF order is formed. In an AF ordered state, net projected moment along the applied field is significantly reduced, and vanishes in the case of collinear AF order, resulting in the observed drop in the Knight shift.

C. Nature of the broken symmetry

In Fig. 5, we plot 23 Na NMR spectra of Ba₂Na_{1-x}Ca_xOsO₆ for x = 0 [Fig. 5(a)]; x = 0.125 [Fig. 5(b)] at 11 T; and x = 0.9 [Fig. 5(c)] at 7 T. The cubic paramagnetic (PM) state is characterized by the narrow symmetric spectra, as expected in the highly symmetric cubic PM phase. The BLPS arises in the intermediate temperature range and is marked by asymmetric spectra with a more pronounced tail at lower frequencies. At low temperatures, in the magnetically ordered phase, the BLPS phase coexists with magnetism revealed by asymmetry of the NMR spectra. As elaborated in the Sec. II C and Appendix IIC, a cubic local environment at the nuclear site must lead to a symmetric spectrum, while only noncubic local symmetries, such as tetragonal or orthorhombic, can generate asymmetric lineshapes. We note that the NMR spectra in the high-temperature PM phase are both narrow and symmetric for all concentrations investigated in this paper. This observation, excludes the possibility that local deviations of cubic symmetry observed at lower temperature are trivial consequence of the Ca/Na alloying, as such effect should be detectable at higher temperatures as well.

We have performed detailed simulations of the 23 Na NMR powder pattern spectra in the presence of a quadrupolar interaction with the electric field gradient (EFG) and an anisotropic Knight shift \mathbb{K} (see Sec. II C and Appendix II C), following the notation of Ref. [58]. We find that above T_N , in the PM and BLPS phases, the resulting powder NMR spectra must reflect the symmetry of the \mathbb{K} and EFG tensors. Therefore, the shape of the NMR spectra provides precise information about any deviation from the cubic symmetry. Indeed, our systematic analysis of the measured spectra demonstrates that the best fits can only be achieved by using orthorhombic distortions, in agreement with findings in Ba_2NaOsO_6 single crystals [13].

In Figs. 5(b) and 5(c) we illustrate representative results of our 23 Na NMR powder spectra simulations in the BLPS phase (details of the simulation are given in Appendix II C). By fitting the powder spectra, we deduce that the EFG and $\mathbb K$ tensors are orthorhombic and collinear to one another. These findings reveal that the main signature of the BLPS phase is not only the cubic symmetry breaking, but also the concurrent development of a collinear $\mathbb K$ anisotropy, indicating that the BLPS is a consequence of a multipolar order formation. That is, the deduced $\mathbb K$ anisotropy implies that the BLPS does not consist of a simple structural distortion but rather involves distortions of magnetic super-exchange paths, plausibly induced by a formation of a multipolar ordering. Furthermore, this is compatible with the fact that deviations of the magnetic

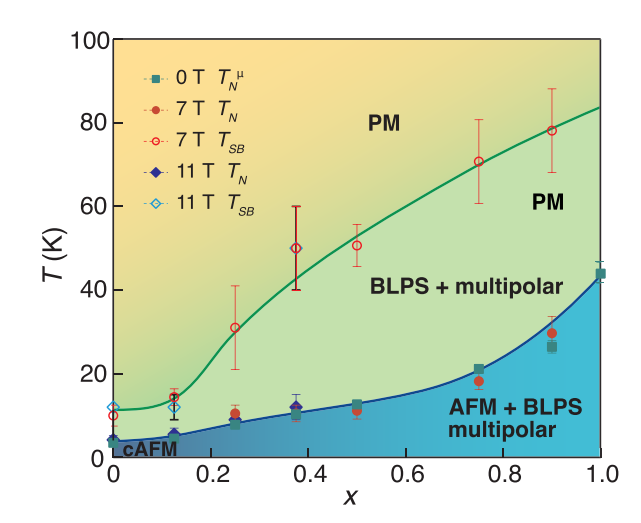


FIG. 7. Phase diagram of $Ba_2Na_{1-x}Ca_xOsO_6$. Solid markers denote the magnetic transition to the canted AFM and collinear AFM state for zero-field μSR and high-field NMR measurements. Open markers denote structural transitions into the BLPS phase. Solid lines serve as a guide to the eye.

susceptibility from the Curie-Weiss behavior are observed at temperatures well above T_N . That is, these deviations occur at temperatures $\approx T_{SB}$, as depicted in Fig. 8 in Appendix A. Therefore, the BLPS is most likely an anisotropic multipolar phase.

D. Phase diagram

Both T_{SB} and T_N obtained from ²³Na NMR at 7 T and 11 T are displayed in the temperature versus doping phase diagram plotted in Fig. 7. The results show that the BLPS phase, a precursor to the magnetic state, is an intrinsic characteristic of these Mott-insulating metal oxides and persists to higher temperature, up to about 80 K, when approaching the $5d^2$ configuration. This orthorhombic local point distortion of the octahedra is a clear signature that these materials are intrinsically dominated by low-temperature anisotropic spin-lattice interactions, an essential ingredient to be included in any microscopic quantum theory of Dirac-Mott insulators.

V. CONCLUSIONS

We have performed a microscopic investigation of the transformation of a $5d^1$ double perovskite Mott insulator into a $5d^2$ configuration by charge doping. We observed that the system remains insulating while the NMR linewidth (Gaussian blur) increase as doping approaches $x \to 1$. These findings indicate that the injected charges are not uniformly distributed into the $5d^1$ double perovskite, rather they are inhomogeneously trapped, most likely on the Os sites that convert the system to $5d^2$ configuration. The formation of polarons, quasiparticles formed by the coupling of excess charge with ionic vibrations, has been recently proposed as another plausible mechanism for dopant trapping [24,59].

Our magnetization measurements reveal that AF exchange interactions become enhanced as charge doping alters its configuration from $5d^1 \rightarrow 5d^2$. Furthermore, detailed analysis of

the NMR shift and lineshapes in the magnetically ordered state reveals that magnetism coexists with the BLPS phase, and that it evolves from a canted AFM state to a collinear AF for dopant levels exceeding (x > 0.1). In $5d^1$ Ba₂NaOsO₆, a cAFM order was identified to arise from the BLPS, as a result of the interplay of electron correlations and the degree of Jahn-Teller distortions [53]. Therefore, the breaking of cubic symmetry in Ba₂NaOsO₆ destabilizes the collinear AF state in favor of the cAFM state. Our finding that a collinear AF order coexists with the BLPS for x > 0.1 suggests that the theoretical results of Ref. [53] need to be extended to include effects of enhanced electron correlations, SOC, and Jahn-Teller interaction with doping. Therefore, our results show that charge doping profoundly alters the interplay between spin-exchange interactions, Jahn-Teller distortions, and electronic correlations as the system evolves away from the $5d^1$ configuration, and provides pertinent constraints to guide the development of microscopic models of Mott insulators with SOC.

Through a comprehensive analysis of the temperature dependence of the NMR shift and lineshapes, we established that a BLPS phase occupies an increasing portion of the (H-T)phase diagram with increased doping. This finding is seemingly in contradiction with those in Refs. [21,47] reporting a single transition into Néel order at $T^* \approx 50$ K, and no evidence of deviations from cubic symmetry in Ba₂CaOsO₆. It was proposed that these rather unusual results below T^* in [21] may be reconciled by the emergence of timereversal symmetry breaking, ferro-octupolar order [16,22,49]. Although the diffraction data in [21] is high intensity, it is not obvious that its resolution was sufficient to detect a small deviations from cubic symmetry like those reported here and/or seen in Ba₂MgReO₆ [19]. Improved resolution in [47] might still not be good enough to detect a deviation from cubic symmetry. Moreover, it is more difficult to reconcile the inference of cubic symmetry from high-resolution synchrotron powder XRD data collected on Ba₂CaOsO₆ at 20 K [21]. This finding suggests that the local distortions are not coherent over the diffraction length scale. We cannot undeniably exclude the other more trivial explanations that include the possibility that the distortions are present in the x = 0.9 sample but not in the x = 1.0 (Ba₂CaOsO₆) one, and/or they are so subtle that even in high-resolution synchrotron data they remain undetectable. Nevertheless, if the local static deviations from cubic symmetry in the BLPS, as reported here, are not sufficiently coherent to drive a long-range distortion observable in scattering experiments, then an antiferro order of active quadrupoles within the e_g doublet identified in [50] can be possibly identified as a competing phase. That is, if the distortions inherent to the BLPS phase are present, then the quadrupolar AFM phase is more stable. This is in contrast with the case when the system preserves cubic symmetry and acquires a octupolar-FM order. Since these two multipolar phases are very close in energy, it could be that small perturbations induce tiny local distortions and promote the onset of the quadrupolar AFM. Even though, a dynamical Jahn-Teller distortions could exist in the ferro-octupolar phase, our current NMR measurements were designed to probe static BLPS effects and as such support quadrupolar AFM scenario. Future measurements sensitive to the dynamical effects and performed on x = 1 pure compounds will be instrumental in determination of the precise nature of the multipolar order.

Our microscopic data clearly shows that in the limit of $x \rightarrow$ 1, the system exhibits local deviations from cubic symmetry below $T_{SB} \sim 80$ K, while a Néel AF order develops below $T_N \sim 40$ K, with a staggered moment of 0.05 μ_B . Therefore, our observations of the broken local cubic symmetry indicate that the BLPS phase is driven by a formation of a multipolar order [57], most likely of the antiferro-quadrupolar type [18,50], because ferro-octupolar order preserves cubic symmetry. The conclusion that the BLPS phase is of antiferro-quadrupolar type is supported by two additional findings. Firstly, the BLPS phase is characterized by an anisotropic NMR shift tensor in addition to orthorhombic local distortions. Secondly, the alluded inhomogeneous nature of the charge doping promotes quadrupolar four-spin exchange interactions, making quadrupolar phase more stable, and implying that the onset of the BLPS-quadrupolar phase should occur at a higher temperature as doping increases, consistent with presented observations. Our NMR measurements indicate that local distortions, induced by the antiferro-quadrupolar order, are inhomogeneous, i.e., consists of areas of distortions of different magnitude. Such local distortions, seen by NMR, do not coherently order and give rise to diffraction peaks here in the way they do in the related $5d^1$ compound, Ba₂MgReO₆ [19].

One could argue that ferro-octupolar order is not observed in our doped samples simply because inhomogeneous dopants can induce local strain, consequently leading to a breaking of the local cubic symmetry. However, local strain is predicted to suppress the octupolar ordering temperature because it induces a transverse field in the octupolar ordering direction, which promotes quantum fluctuations [22], and thus is in contradiction with phase diagram presented in Fig. 7. Therefore, our NMR findings support emergence of an antiferro-quadrupolar order in the doped $5d^1 \rightarrow 5d^2$ double perovskites. The quadrupolar phase most likely arises as lattice distortions amplify the quadrupolar interactions via Jahn-Teller interactions.

Aforementioned recent theoretical study of the impurity effects in the pure $5d^2$ limit in Ref. [57], provides an alternative explanation on the nature of the multipolar order based on the analysis of our NMR data for x > 0.9. Precisely, it is deduced that our data indicates that multipolar order established in the vicinity of the pure $5d^2$ limit is an octupolar one. That is, Na dopants cluster into regions of pairs (or more) of neighboring Na impurities, which lowers the point group symmetry and induces local quadrupoles. These Na clusters induce strain on the local quadrupoles. This strain in turn breaks time-reversal symmetry inducing octuples with finite dipolar moments. At higher temperatures these octuples form short-range order as Na cluster that induce octuples are far apart. On lowering the temperature, long-range octupolar order with LRO magnetism emerges from ordering of the local dipolar moment on octupoles. This picture naturally explains our observation that BLPS onsets at higher temperature than the LRO magnetism, which at first glance might seem in contradiction with presence of the octupolar order [5,16,60]. However, such inhomogeneous form of magnetism for x > 0.9, arising from local nonuniform multipolar order, can arise not only from impurity induced strains but from other intricate effects of spin-orbit entanglement such as those discussed in Ref. [24,53]. As alluded earlier, our current paper implies that the nature of the multipolar order is most likely of the antiferro-quadrupolar type for x < 1. However, we cannot exclude the possibility that the ferro-octupolar phase onsets as $x \to 1$. This issue will be addressed in our future work.

ACKNOWLEDGMENTS

We are thankful to D. Fiore Mosca, P. Santini, Brad Marston, and A. Paramekanti for enlightening discussions. This work was supported in part by U.S. National Science Foundation (NSF) Grant No. DMR-1905532 (V.F.M.), the NSF Graduate Research Fellowship under Grant No. 1644760 (E.G.), NSF Materials Research Science and Engineering Center (MRSEC) Grant No. DMR-2011876 (P.M.T. and P.M.W.), PRIN2022 Project No. 202243JHMW (S.S.), and University of Bologna (S.S. and P.C.F.). Part of this work is based on experiments performed at the Swiss Muon Source $S\mu S$, Paul Scherrer Institute, Villigen, Switzerland. The study at the NHMFL was supported by the National Science Foundation under Cooperative Agreement no. DMR-1644779 and the State of Florida.

APPENDIX A: CURIE-WEISS BEHAVIOR

Here we plot the individual fits of the magnetic susceptibility (see Sec. II B) to the Curie-Weiss (CW) linear temperature behavior. The individual CW fittings are shown in red in Fig. 8 for (a) x = 0, (b) x = 0.25, (c) x = 0.5, (d) x = 0.9, and (e) x = 1.0. The extracted CW temperature (θ_{CW}) and effective moment per formula (μ_{eff}) for the corresponding fits are displayed in the inset of Fig. 3(b).

APPENDIX B: HYPERFINE TENSOR

The diagonal components of the hyperfine coupling tensor were determined in the PM phase from Clogston-Jaccarino plots of all of the doping concentrations, as shown in Fig. 9(b). For the off-diagonal values, the symmetry of the tensor is taken to be that obtained for the BNOO single crystal in Ref. [13]. The tensor form was found to be given by

$$A = \begin{pmatrix} aa & ab & ac \\ -ab & bb & bc \\ ac & bc & cc \end{pmatrix}.$$
 (B1)

APPENDIX C: SIMULATION OF THE NMR SPECTRA

Here, we discuss details of the χ^2 fit of the measured ²³Na NMR powder spectra to the simulated powder pattern spectra for nuclear spin I=3/2 subject to the quadrupolar interaction and an anisotropic Knight shift. The powder average was computed numerically by a modified program based on a Fortran subroutine written by D. W. Alderman [61].

Model. The lineshape is modeled by three distinct components:

(1) An anisotropic Knight shift tensor \hat{K} with arbitrary orientation relative to the crystal axes. The total magnetic field at the nucleus is written as

$$\vec{H}_{\text{nuc}} = \vec{H}_0 + \delta \vec{H}_{\text{nuc}} = (1 + \hat{K})(\vec{H}_0).$$
 (C1)

For an orientation defined by the unit vector $\mathbf{u} = \vec{H}_0/H_0$, the effective shift of the resonance line $K_{\rm eff}$, defined as $H_{\rm nuc} = (1 + K_{\rm eff})H_0$, is calculated to first order as $K_{\rm eff} = \mathbf{u} \cdot \hat{K}\mathbf{u}$. The symmetric tensor \hat{K} is parameterized by its principal components, K_x , K_y , K_z , and three Euler angles, ϕ , ϕ , ψ , defining the orientation of the principal axes of \hat{K} relative to those of the EFG (i.e., the crystal reference frame).

(2) The quadrupolar interaction is expressed as

$$H_Q = \frac{h\nu_Q}{6} \left[3I_z^2 - I(I+1) + \frac{\eta}{2}(I_+^2 + I_-^2) \right]$$
 (C2)

in the crystal reference frame. Here ν_Q (which coincides with the zero-field NQR frequency only if $\eta=0$) is a coupling parameter in units of frequency. H_Q is treated as a perturbation of the dominant Zeeman interaction, $H_Z=\gamma(1+\hat{K})\vec{H}_0$, and the satellite lines are calculated to second order in perturbation theory.

(3) Incoherent Gaussian line broadening σ calculated by the convolution with a Gaussian, which reflects magnetic inhomogeneities (i.e., the inhomogeneity of \hat{K}). Quadrupolar inhomogeneities can be modeled in principle by a Gaussian broadening of only the satellite lines (since the central $1/2 \leftrightarrow -1/2$ transition is unaffected by H_Q to first order). However, we determined that this quadrupolar inhomogeneous broadening is negligible in this case. Nevertheless, we label this kind of line broadening as "incoherent" since the powder average of the interactions is calculated first and then the resulting spectra are broadened (hence, any possible correlation between local values of K and ν_Q can be/is neglected).

Fit. In the fit of the data, \hat{K} is conveniently represented by its isotropic component, $K_{\rm iso} = 1/3 {\rm Tr} \hat{K}$, and two independent traceless components, $\hat{K}_{\rm cyl}$ and $\hat{K}_{\rm rhom}$. The isotropic Zeeman frequency $\nu_{\rm iso} = \gamma/2\pi(1+K_{\rm iso})H$ is determined directly as a fitting parameter, so $K_{\rm iso}$ can be extracted if the reference frequency $^{23}\nu$ of $^{23}{\rm Na}$ is known in the given applied field. The other components, $K_{\rm cyl}$ and $K_{\rm rhom}$, are defined as follows:

$$K_{\rm x} = -1/2K_{\rm cyl} + 1/2K_{\rm rhom} + K_{\rm iso},$$

 $K_{\rm y} = -1/2K_{\rm cyl} - 1/2K_{\rm rhom} + K_{\rm iso},$ (C3)
 $K_{\rm z} = K_{\rm cyl} + K_{\rm iso}.$

The fitting consistently returned best-fit Euler angles $\phi = 0$, $\theta = 0$, $\psi = 0$, which implies that the Knight shift principal axes coincide with those of EFG. The best-fit simulated NMR spectra in the intermediate temperature range (in the BLPS state for $T_N < T_{SB}$) are displayed in Figs. 5(d)–5(f). The corresponding fitting parameters are displayed in Table I. Throughout the entire doping range, the best-fit EFG and \hat{K} tensors are consistently orthorhombic and collinear to each other. The inaccuracy of the fit is likely due to inhomogeneities in the interaction, which are not properly accounted for by the model of incoherent broadening.

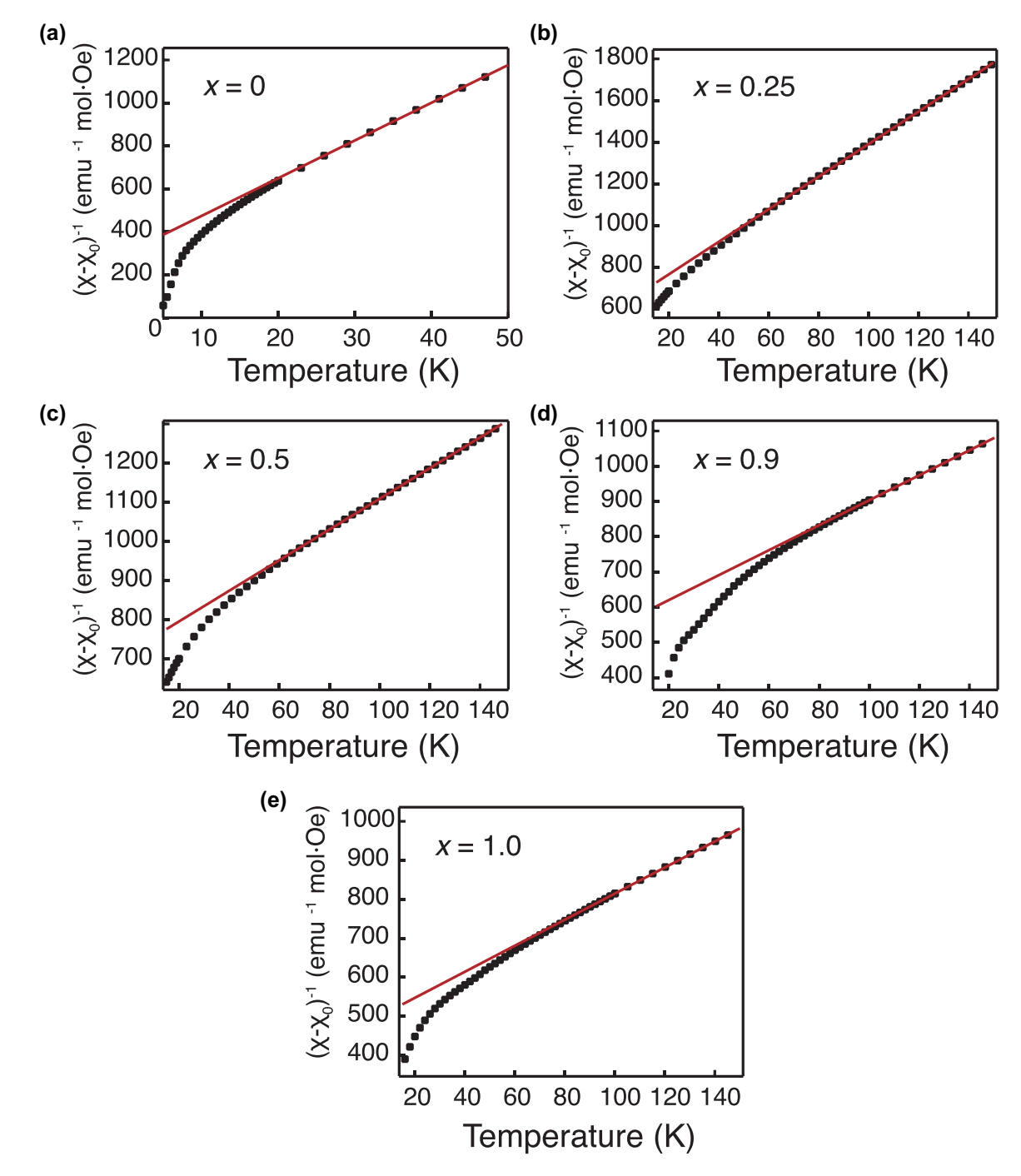


FIG. 8. Curie-Weiss fittings of magnetic susceptibility. The red lines denote the results of Curie-Weiss (CW) fittings for (a) x = 0, (b) x = 0.25, (c) x = 0.5, (d) x = 0.9, and (e) x = 1.0 in the PM state. The extracted CW temperature (θ_{CW}) and effective moment per formula unit (μ_{eff}) are displayed in the inset to Fig. 3(b).

We note that one would naively expect that a $5d^2$ (Os⁶⁺) distorts in a different way than a $5d^1$ (Os⁷⁺), especially because the low-temperature NMR data for the x=0 (significantly asymmetric) and x=0.9 (more symmetric) samples look qualitatively different. However, our detailed analysis of the spectral shapes indicates that no significant variation in the EFG is revealed as doping increases from x=0 (300 kHz) to x=0.9 (280 KHz). Therefore, local distortions are orthorhombic and do not change in nature as a function of doping. It is the asymmetry of the NMR

shift that is significantly suppressed as doping increases thus leading to overall more symmetric NMR lineshape for x = 0.9.

APPENDIX D: POWDER NMR SPECTRUM SIMULATION OF COLLINEAR CANTED AFM MODEL

This simulation is constructed by using a two sublattice spin-staggered pattern (similar to the one used for Ba₂NaOsO₆ (BNOO) single crystal in Ref. [13]) and calcu-

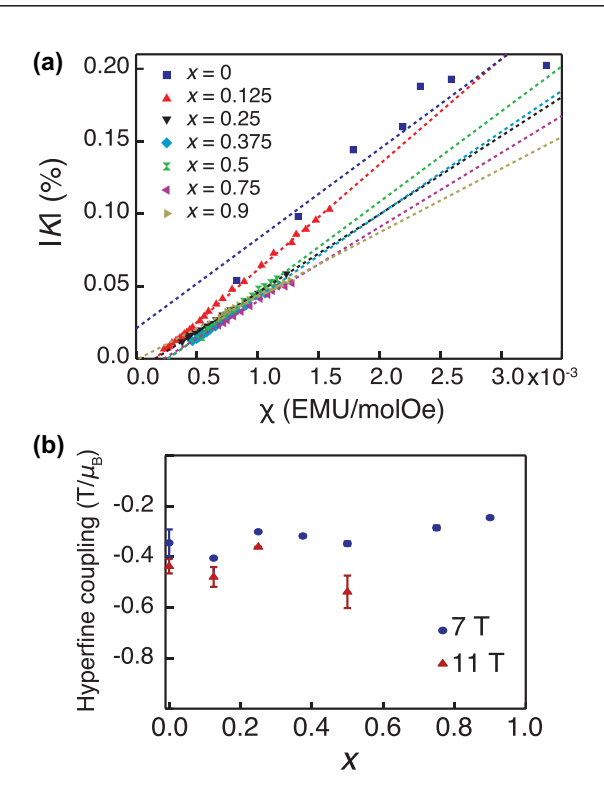


FIG. 9. Hyperfine coupling constant determination. (a) 23 Na Clogston-Jaccarino plot with temperature as implicit parameter for each point. Solid lines denote linear fit to the data, with a fitting range from the highest temperature available to the magnetic transition temperature T_N for each doping concentration. (b) Hyperfine coupling constant extracted from linear fits shown in the top figure.

lating the local field distribution at two distinct Na sites when the sample is oriented at an arbitrary angle (θ_Q, ϕ_Q) relative to the external field direction, where (θ_Q, ϕ_Q) are the polar angles between the external field coordinate and the EFG principle coordinate (which is same as the crystal coordinate for BNOO since the principle axes of EFG tensor are aligned with the crystal axes). The local magnetic field at the Na sites are then calculated according to

$$H_{\text{loc}} = \hat{\mathbf{h}} \cdot \sum_{i} \mathbb{A}_{i} \cdot \mathbf{S}_{i} + \frac{\omega_{Q}}{\gamma} (m - 1/2)$$

$$\times (3\cos^{2}\theta_{Q} - 1 + \eta \sin^{2}\theta_{Q}\cos 2\phi_{Q}), \tag{D1}$$

where the first term accounts for the Zeeman and the second for the quadrupolar interaction. The summation includes the six nearest-neighbor sites around the Na atoms and the hyperfine coupling tensor \mathbb{A}_i (in the units of $[T/\mu_B]$) is same

for all the nearest-neighbor sites with S_i being the local spin moments (in the units of $[\mu_B]$). The relationship between the Knight shift tensor \mathbb{K} and hyperfine tensor \mathbb{A} can be written as $\mathbb{K}_i = \mathbb{A}_i S_i / H_0$. The local fields generated by quadrupolar effects are then added using fixed EFG parameters obtained from fitting to the spectra measured in the intermediate temperature range $(T_N < T_{SB})$. The powder sample average was performed by integrating over the 4π solid angle while varying the orientation of the applied magnetic field. A random sampling on the 4π solid angle is done by sampling the polar angle (θ_O, ϕ_O) , which satisfies $\theta_O = \arccos(1 - 2\zeta)$ and $\phi_O =$ $2\pi \eta$, respectively. Here ζ and η are two numbers randomly generated between 0 and 1, with a total sampling number of 50 000. The calculated local fields when the external magnetic field is oriented uniformly in the 4π solid angle are then plotted as a histogram and convoluted with a Gaussian function to get the final simulated spectrum (in MHz) to compare with the experimental data.

There are several factors that go into the construction of the simulated spectrum that are important to obtain the correct results, such as, the spin arrangement, and the net/effective moment when the field is at an arbitrary angle relative to the sample, the hyperfine tensor values, etc. Below are some detailed description of how these factors are implemented in the current simulation code.

Spin arrangement pattern. The spin directions for this simulation are based on the BNOO single crystals in-plane canted AFM [110] pattern, as shown in Ref. [13], Fig. 4(b). Sublattice A and B are staggered by approximately 67° relative to the easy axis [110] on two neighboring layers. Based on the diagonal rotation pattern of BNOO, the two sublattices of spins rotate with the field direction in the same plane while keeping the same canting angles when the field direction is rotated from [110] to [001].

Extending to the powder cases, the field dependence of the spin-sublattice directions is assumed to be the same as in the case of the BNOO single crystal for the entire 4π solid angle, not only when the field direction is along the diagonal rotation directions but also when the field is rotated in the xy plane. This means that the staggered spins keep the same canting angle relative to the field direction when they are placed in different orientations relative to the external field, as shown in Fig. 10.

Field dependence of net moment. The field dependence of the net moment on the BNOO, single crystal, Fig. 3 in Ref. [43], is very important to the fit of the diagonal rotation pattern of the averaged field. Here, the ordered moment angle dependence along the [001], [111], and [110] high

TABLE I. ²³Na powder NMR spectra simulation fitting results.

Ca %	T (K)	v _{iso} (MHz)	ν _Q (kHz)	η	σ (kHz)	$K_{\rm cyl} (10^{-3})$	$K_{\text{rhom}} (10^{-3})$
0	9	123.6516(6)	301(3)	0.92(2)	41(2)	-2.253(14)	-0.681(17)
12.5	9	123.7798(9)	282(4)	0.51(3)	49(2)	-1.65(3)	-0.38(7)
25	11	123.8299(5)	345(2)	1.00(2)	64(1)	-2.483(14)	-1.29(2)
37.5	15	123.8177(10)	343(3)	0.79(2)	42(2)	-2.344(19)	-0.83(6)
50	17	123.8031(7)	356(3)	0.658(4)	39(1)	-2.389(32)	-0.293(11)
90	40	123.8590(2)	279.5(3)	1.00(3)	27.2(5)	-1.918(3)	-1.252(11)

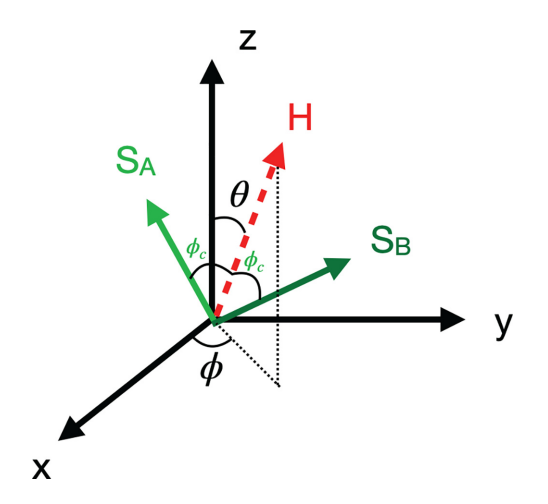


FIG. 10. Schematic graph showing the staggered spin model pattern relative to an arbitrary field direction. The red arrow H represents the direction of external magnetic field. S_A and S_B represent the spin moment orientations on the two sublattices. The angles θ and ϕ refer to the angles θ_Q and ϕ_Q , which are the polar angles of the field direction relative to the EFG (and crystal) coordinate.

symmetry axes can be fitted and described numerically by $M_{\text{ordered}} = 0.2 \, \mu_B \cdot \alpha(\theta)$, where $0.2 \, \mu_B$ is the largest ordered moment when the crystal's [110] axis is aligned with the external magnetic field and $\alpha(\theta)$ is the numerically fitted angle dependence relationship. For the doped powder samples, the effective moment values are taken from the magnetization measurements [inset to Fig. 1(b)].

Effective moment values. For the BNOO single crystal, the effective moment is $0.6\,\mu_B$, corresponding to three times its largest ordered moment of $0.2\,\mu_B$ when its [110] axis is aligned with the external magnetic field. The same is obtained for the BNOO powder sample. So, the effective moment for all of the doped samples in the simulation are taken to be the values shown in the inset to Fig. 1(b) in the main text. These effective moments are used in combination with the field dependence of the net moment as described in the section above, meaning that $\mathbf{S}_i = \mathbf{S}_{\rm eff} \cdot \alpha(\theta)$.

Quadrupolar effect. The quadrupolar effect is added to the two distinct Na sites after obtaining their local field from $H_{\rm loc} = \sum_i \mathbb{A} \cdot \vec{S}_i$. The EFG parameters and principle axes are fixed, taken from the values shown in Table I. The corresponding local fields generated from the quadrupolar splitting are written as $\delta_q = \frac{1}{2} \nu_Q (3 \cos^2 \theta - 1 + \eta \sin^2 \theta \cos^2 \phi)$, where θ and ϕ describe the orientation of the external field relative to the EFG principle axes. These quadrupolar local fields are combined with local field generated from the hyperfine interactions to obtain the local field histogram, i.e., spectra plotted in Fig. 11.

Results. In Fig. 11 we plot the optimization results for all doping concentrations. The optimization solver used in Python is "Nelder-Mead". Initial conditions are first tuned manually.

In the plots in Fig. 11, histogram is shown in blue and the orange line represents the generated spectrum after convoluted with a Gaussian function. Both the simulated (or-

TABLE II. ²³Na powder NMR spectra simulation fitting results for spectra taken at low temperatures ($T=1.4\,\mathrm{K}$ for all x except for x=0.25 acquired at $T=4.2\,\mathrm{K}$) in the magnetically ordered state. ϕ_{stg} represents the staggered angle of the two sublattice spins relative to the external field direction. σ represents the Gaussian blur. $\mathbb A$ is the hyperfine coupling tensor.

X	$\phi_{ m stg}$ $^{\circ}$	σ (MHz)	$\mathbb{A}(T/\mu_B)$
0	69.8	0.19	$\begin{pmatrix} 0.39 & -0.11 & -0.14 \\ 0.11 & 0.37 & 0.15 \\ -0.14 & 0.15 & 0.37 \end{pmatrix}$
0.125	85.6	0.25	$ \begin{pmatrix} 0.50 & -0.05 & -0.09 \\ 0.05 & 0.43 & 0.04 \\ -0.09 & 0.04 & 0.47 \end{pmatrix} $
0.25	87.7	0.16	$\begin{pmatrix} 0.39 & -0.04 & -0.04 \\ 0.04 & 0.28 & 0.05 \\ -0.04 & 0.05 & 0.36 \end{pmatrix}$
0.375	87.5	0.23	$\begin{pmatrix} 0.35 & -0.03 & -0.04 \\ 0.03 & 0.30 & 0.04 \\ -0.04 & 0.04 & 0.33 \end{pmatrix}$
0.50	88.4	0.27	$\begin{pmatrix} 0.58 & -0.03 & -0.03 \\ 0.03 & 0.50 & 0.05 \\ -0.03 & 0.05 & 0.51 \end{pmatrix}$
0.90	87.7	0.51	$\begin{pmatrix} 0.36 & -0.03 & -0.04 \\ 0.03 & 0.33 & 0.05 \\ -0.04 & 0.05 & 0.33 \end{pmatrix}$

ange) and data/measured spectrum (green) are normalized by their amplitude.

The simulation results show that the staggered angle changes from ${\sim}68^{\circ}$ to ${\sim}90^{\circ}$ with increased Ca doping. This could explain the doping dependence on the Knight shift.

The Gaussian blur, as determined by fitting, significantly increases for x > 0.2 to allow for a good fit to the wide measured linewidth. However, the calculated local field distribution, represented by the histogram only, does not show the same significant increase. This indicates that there might be other sources of the inhomogeneous broadening, besides that arising from the two sublattice magnetic state, to account for the large linewidth for x > 0.2.

Since the current model treats the effective moments for all of the doping samples as fixed input parameters, the calculated doping evolution of the Knight shift and the linewidth are compatible with that of the effective moments. For 0 < x < 0.125, the decrease in the Knight shift is because of the staggered angle changes from $\sim 67^{\circ}$ to $\sim 85^{\circ}$. The decrease in the linewidth can be accounted for by the decrease of the off-diagonal components of the their hyperfine coupling tensor, even though the effective moments increase in this region. Above x = 0.25 doping, the off-diagonal components are about constant up to x > 0.9, and the increase in the linewidth in this region comes from the increase of the effective moments.

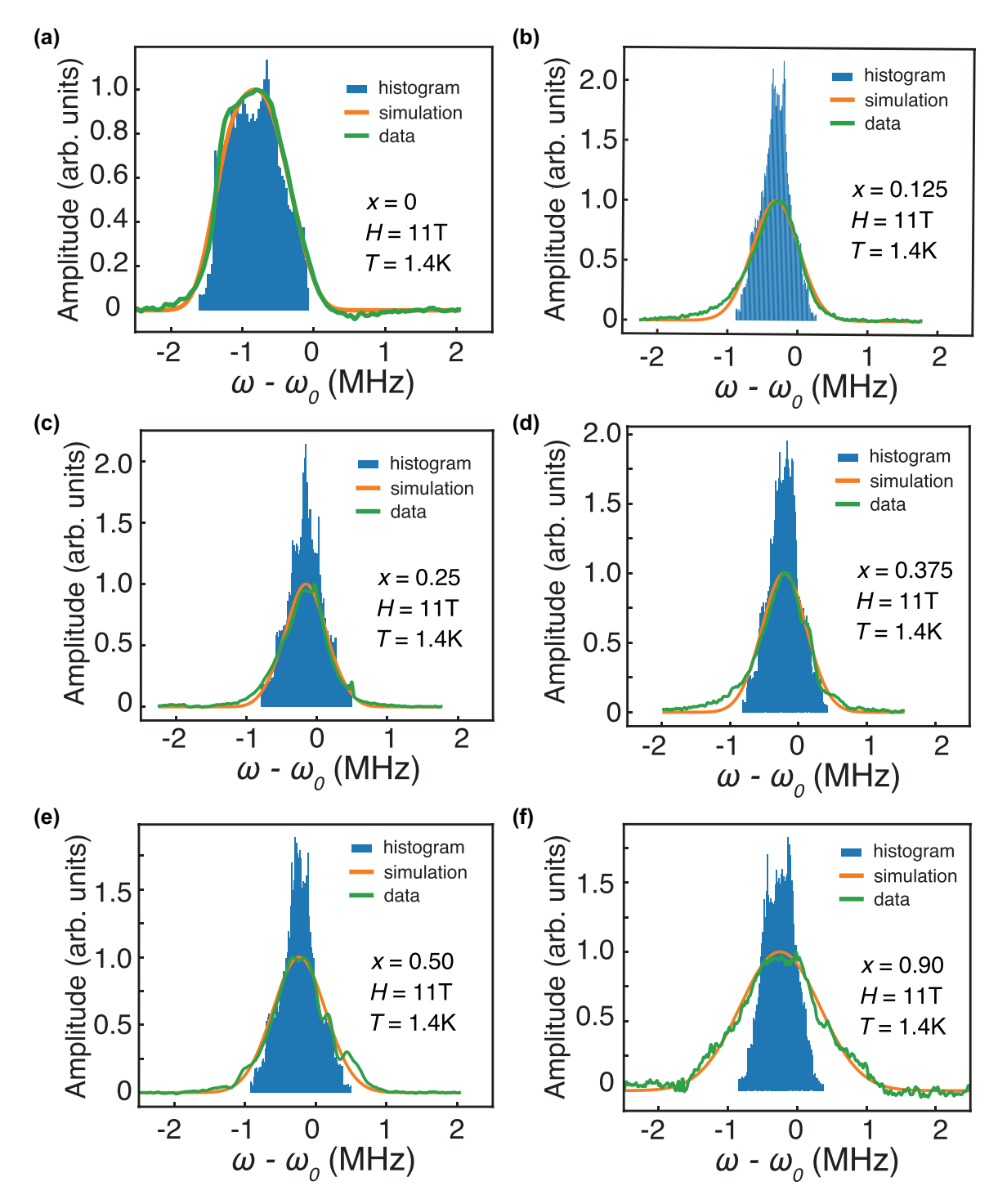


FIG. 11. 23 Na powder NMR spectra simulation results for $Ba_2Na_{(1-x)}Ca_xOsO_6$. Spectra shown at H=11 T in the low-temperature magnetic phase for (a) x=0, (b) x=0.125, (c) x=0.25, (d) x=0.375, (e) x=0.50, and (f) x=0.90. Green lines represent measured NMR spectra, blue lines represent simulated histogram and orange lines represent fitted spectra. The simulation fit parameters of these NMR spectra are displayed in Table II.

^[1] W. Witczak-Krempa, G. Chen, Y. B. Kim, and L. Balents, Annu. Rev. Condens. Matter Phys. 5, 57 (2014).

^[2] G. Jackeli and G. Khaliullin, Phys. Rev. Lett. **102**, 017205

^[3] F. O. Nigmatulin, I. A. Shelykh, and I. V. Iorsh, Phys. Rev. Res. 3, 043016 (2021).

^[4] T. Takayama, J. Chaloupka, A. Smerald, G. Khaliullin, and H. Takagi, J. Phys. Soc. Jpn. 90, 062001 (2021).

^[5] D. I. Khomskii, ECS J. Solid State Sci. Technol. 11, 054004

^[6] G. Chen, R. Pereira, and L. Balents, Phys. Rev. B 82, 174440 (2010).

- [7] G. Chen and L. Balents, Phys. Rev. B 84, 094420 (2011).
- [8] C. Svoboda, W. Zhang, M. Randeria, and N. Trivedi, Phys. Rev. B 104, 024437 (2021).
- [9] H. Ishizuka and L. Balents, Phys. Rev. B 90, 184422 (2014).
- [10] R. Cong and V. F. Mitrović, Bull. Am. Phys. Soc. F54.0000 (2021).
- [11] E. S. Sørensen, A. Catuneanu, J. S. Gordon, and H.-Y. Kee, Phys. Rev. X 11, 011013 (2021).
- [12] Q. Luo, P. P. Stavropoulos, J. S. Gordon, and H.-Y. Kee, Phys. Rev. Res. 4, 013062 (2022).
- [13] L. Lu, M. Song, W. Liu, A. P. Reyes, P. Kuhns, H. O. Lee, I. R. Fisher, and V. F. Mitrović, Nat. Commun. 8, 14407 (2017).
- [14] A. S. Cavichini, M. T. Orlando, J. B. Depianti, J. L. Passamai, F. Damay, F. Porcher, and E. Granado, Phys. Rev. B 97, 054431 (2018).
- [15] A. Mansouri Tehrani and N. A. Spaldin, Phys. Rev. Mater. 5, 104410 (2021).
- [16] A. Paramekanti, D. D. Maharaj, and B. D. Gaulin, Phys. Rev. B 101, 054439 (2020).
- [17] S. Voleti, D. D. Maharaj, B. D. Gaulin, G. Luke, and A. Paramekanti, Phys. Rev. B 101, 155118 (2020).
- [18] D. Churchill and H.-Y. Kee, Phys. Rev. B 105, 014438 (2022).
- [19] D. Hirai, H. Sagayama, S. Gao, H. Ohsumi, G. Chen, T.-H. Arima, and Z. Hiroi, Phys. Rev. Res. 2, 022063(R) (2020).
- [20] R. D. Johnson, I. Broeders, K. Mehlawat, Y. Li, Y. Singh, R. Valentí, and R. Coldea, Phys. Rev. B 100, 214113 (2019).
- [21] D. D. Maharaj, G. Sala, M. B. Stone, E. Kermarrec, C. Ritter, F. Fauth, C. A. Marjerrison, J. E. Greedan, A. Paramekanti, and B. D. Gaulin, Phys. Rev. Lett. 124, 087206 (2020).
- [22] S. Voleti, A. Haldar, and A. Paramekanti, Phys. Rev. B 104, 174431 (2021).
- [23] J. K. Kesavan, D. Fiore Mosca, S. Sanna, F. Borgatti, G. Schuck, P. M. Tran, P. M. Woodward, V. F. Mitrović, C. Franchini, and F. Boscherini, J. Phys. Chem. C 124, 16577 (2020).
- [24] L. Celiberti, D. F. Mosca, G. Allodi, L. V. Pourovskii, A. Tassetti, P. C. Forino, R. Cong, E. Garcia, P. M. Tran, R. D. Renzi et al., arXiv:2306.15757
- [25] M. Imada, A. Fujimori, and Y. Tokura, Rev. Mod. Phys. 70, 1039 (1998).
- [26] P. A. Lee, N. Nagaosa, and X.-G. Wen, Rev. Mod. Phys. 78, 17 (2006).
- [27] Z.-X. Li, S. A. Kivelson, and D.-H. Lee, npj Quantum Mater. 6, 36 (2021).
- [28] H.-C. Jiang and S. A. Kivelson, Proc. Natl. Acad. Sci. USA 119, e2109406119 (2022).
- [29] E. Fradkin, S. A. Kivelson, and J. M. Tranquada, Rev. Mod. Phys. 87, 457 (2015).
- [30] S. Middey, J. Chakhalian, P. Mahadevan, J. Freeland, A. J. Millis, and D. Sarma, Annu. Rev. Mater. Res. 46, 305 (2016).
- [31] Y. Tokura and N. Nagaosa, Science 288, 462 (2000).
- [32] W. Xia, Z. Pei, K. Leng, and X. Zhu, Nanoscale Res. Lett. 15, 9 (2020).
- [33] Y. Feng, Y. Wang, D. M. Silevitch, S. E. Cooper, D. Mandrus, P. A. Lee, and T. F. Rosenbaum, Nat. Commun. 12, 2779 (2021).
- [34] J.-M. Carter, V. Shankar, and H.-Y. Kee, Phys. Rev. B **88**, 035111 (2013).
- [35] T. Han, Y. Wang, J. Yang, L. He, J. Xu, D. Liang, H. Han, M. Ge, C. Xi, W. Zhu *et al.*, Appl. Phys. Lett. **109**, 192409 (2016).

- [36] A. Bandyopadhyay, I. Carlomagno, L. Simonelli, M. Moretti Sala, A. Efimenko, C. Meneghini, and S. Ray, Phys. Rev. B **100**, 064416 (2019).
- [37] M. Vogl, L. T. Corredor, T. Dey, R. Morrow, F. Scaravaggi, A. U. B. Wolter, S. Aswartham, S. Wurmehl, and B. Büchner, Phys. Rev. B 97, 035155 (2018).
- [38] Y. Gao, M. Ashtar, L. Xu, Z. Ouyang, W. Tong, S. Yuan, and Z. Tian, J. Phys.: Condens. Matter 32, 105702 (2020).
- [39] N. Narayanan, D. Mikhailova, A. Senyshyn, D. M. Trots, R. Laskowski, P. Blaha, K. Schwarz, H. Fuess, and H. Ehrenberg, Phys. Rev. B 82, 024403 (2010).
- [40] W. K. Zhu, C.-K. Lu, W. Tong, J. M. Wang, H. D. Zhou, and S. X. Zhang, Phys. Rev. B 91, 144408 (2015).
- [41] K. E. Stitzer, M. D. Smith, and H.-C. zur Loye, Solid State Sci. 4, 311 (2002).
- [42] A. J. Steele, P. J. Baker, T. Lancaster, F. L. Pratt, I. Franke, S. Ghannadzadeh, P. A. Goddard, W. Hayes, D. Prabhakaran, and S. J. Blundell, Phys. Rev. B 84, 144416 (2011).
- [43] A. S. Erickson, S. Misra, G. J. Miller, R. R. Gupta, Z. Schlesinger, W. A. Harrison, J. M. Kim, and I. R. Fisher, Phys. Rev. Lett. 99, 016404 (2007).
- [44] W. Liu, R. Cong, E. Garcia, A. P. Reyes, H. O. Lee, I. R. Fisher, and V. F. Mitrović, Phys. B: Condens. Matter 536, 863 (2018).
- [45] R. Cong, R. Nanguneri, B. Rubenstein, and V. F. Mitrović, Phys. Rev. B 100, 245141 (2019).
- [46] K. Yamamura, M. Wakeshima, and Y. Hinatsu, J. Solid State Chem. 179, 605 (2006).
- [47] C. Thompson, J. Carlo, R. Flacau, T. Aharen, I. Leahy, J. Pollichemi, T. Munsie, T. Medina, G. Luke, J. Munevar *et al.*, J. Phys.: Condens. Matter 26, 306003 (2014).
- [48] S. S. Lovesey and D. D. Khalyavin, Phys. Rev. B **102**, 064407
- [49] L. V. Pourovskii, D. F. Mosca, and C. Franchini, Phys. Rev. Lett. 127, 237201 (2021).
- [50] G. Khaliullin, D. Churchill, P. P. Stavropoulos, and H.-Y. Kee, Phys. Rev. Res. 3, 033163 (2021).
- [51] W. Liu, R. Cong, A. P. Reyes, I. R. Fisher, and V. F. Mitrović, Phys. Rev. B 97, 224103 (2018).
- [52] R. Cong, R. Nanguneri, B. Rubenstein, and V. F. Mitrović, J. Phys.: Condens. Matter 32, 405802 (2020).
- [53] D. Fiore Mosca, L. V. Pourovskii, B. H. Kim, P. Liu, S. Sanna, F. Boscherini, S. Khmelevskyi, and C. Franchini, Phys. Rev. B 103, 104401 (2021).
- [54] A. Abragam, The principles of Nuclear Magnetism (Oxford University Press, Oxford, 1961).
- [55] J. Romhányi, L. Balents, and G. Jackeli, Phys. Rev. Lett. 118, 217202 (2017).
- [56] D. Fiore Mosca, L. V. Pourovskii, and C. Franchini, Phys. Rev. B 106, 035127 (2022).
- [57] S. Voleti, K. Pradhan, S. Bhattacharjee, T. Saha-Dasgupta, and A. Paramekanti, arXiv:2211.07666.
- [58] M.-A. Vachon, G. Koutroulakis, V. F. Mitrović, A. P. Reyes, P. Kuhns, R. Coldea, and Z. Tylczynski, J. Phys.: Condens. Matter 20, 295225 (2008).
- [59] C. Franchini, M. Reticcioli, M. Setvin, and U. Diebold, Nat. Rev. Mater. 6, 560 (2021).
- [60] P. Santini and G. Amoretti, Phys. Rev. Lett. 85, 2188 (2000).
- [61] D. Alderman, M. S. Solum, and D. M. Grant, J. Chem. Phys. 84, 3717 (1986).